ACS Catalysis

pubs.acs.org/acscatalysis Research Article

Cyclometallated Iron(II) Alkoxides in Iron-Catalyzed C−H Activations by Weak *O*-Carbonyl Chelation

Antonis M. Messinis, João C. A. Oliveira, A. Claudia Stückl, and Lutz Ackermann*

Cite This: *ACS Catal.* 2022, 12, 4947−4960 Read Online

ACCESS | Metrics & More | Article Recommendations | Supporting Information

ABSTRACT: Iron catalysts represent an economically attractive tool for C−H activations because of their low costs and low toxicities. Despite an exponential increase of interest in this area, detailed mechanistic understanding remains at a nascent stage. Herein, a detailed investigation of the C−H activation mechanism with $[Fe(PMe_3)_4]$ unraveled an unexpected iron(II) alkoxide intermediate that was fully characterized and was found to be a more active catalyst in phenone-assisted C−H activations with respect to the previously reported *mer*-iron hydride cyclometallated counterpart. Mechanistic studies by stoichiometric experimentation, reaction profiling through electron paramagnetic resonance (EPR) and *in operando* NMR spectroscopy, deuterium labeling, crystallographic analyses, and density functional theory (DFT) calculations provided strong evidence for an oxidative addition of the pivalophenone to a low-valent iron intermediate toward the formation of a transient *fac*-hydride complex, which very quickly rearranges to an iron alkoxide complex. According to detailed DFT studies, it is proposed that the isolated iron(II) alkoxide is a highly reactive precatalyst, which can easily access the on-cycle *fac*-hydride complex, thereby translating into highly efficient catalysis. These mechanistic insights form the basis for further developments in iron-catalyzed C−H activation with prospects for stereoselective transformations.

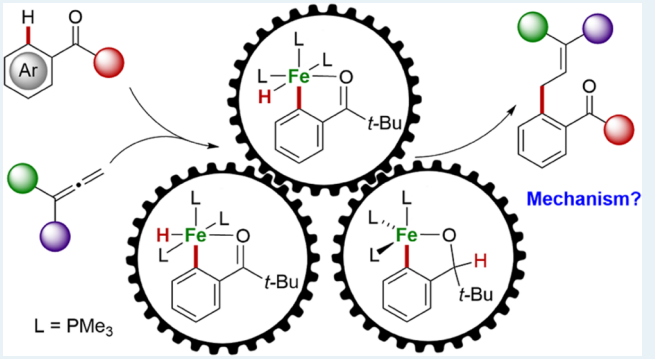

KEYWORDS: *iron, C−H activation, mechanism, allene, computation*

INTRODUCTION

Transition-metal-catalyzed C−H activation has emerged as a transformative platform to enable the direct transformation of otherwise inert C−H bonds.[1−16] As a consequence, C−H activation has experienced explosive growth during the last decade, with applications to molecular[17,18] and natural product syntheses[19] as well as to materials sciences,[20,21] medicinal chemistry,[22−25] and crop protection.[26] Thus, a plethora of C−H activation reactions have been developed, typically requiring precious[27] and potentially toxic[28,29] transition metals, such as palladium,[8] rhodium,[30] and ruthenium.[9,31] Recently, the need to transition toward more sustainable and environmentally benign platforms has triggered the replacement of precious metals by earth-abundant, cost-effective, and typically less toxic alternatives.[32] Among the various first row contenders, iron[7,33−41] stands out due to its extremely low cost,[27] high natural abundance,[42] and lack of significant toxicity.[43]

Despite significant progress in iron-catalyzed C−H activation, the majority of the thus far developed reactions continue to rely on highly reactive Grignard reagents in combination with strong *N*,*N*-bidentate directing groups, reducing the synthetic utility and efficiency of such catalysts.[40,44−54] Thus far, only a limited number of byproduct-free iron-catalyzed C−H activations that utilize weak directing groups have been reported, namely $[Fe_3(CO)_{12}]$-catalyzed alkyne annulation by imines[55] and $[Fe(PMe_3)_4]$-catalyzed hydroarylation,[56−58] as well as a homoallylation of aromatic ketones,[59] thus clearly highlighting the need for further development of this challenging yet promising field.

At the same time, and despite indisputable advances, the mechanistic understanding of C−H activations by organometallic iron catalysis is underdeveloped, indeed lagging far behind the synthetic methodology. Most mechanistic proposals on the mode of operation of iron-catalyzed C−H activation reactions are thus far supported by a limited amount of experimental data. Currently, only a few in-depth studies have been reported, namely on the arylation, alkylation, and allylation of aromatic amides with triazole[51,60,61] and quinoline[62] directing groups and on the

Received: February 12, 2022
Revised: March 29, 2022
Published: April 12, 2022

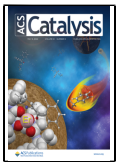

https://doi.org/10.1021/acscatal.2c00772
ACS Catal. 2022, 12, 4947−4960

hydroarylation of allenes enabled by weak *O*-coordination (Scheme 1).[58] In the former studies, the mechanistic manifold proposed was supported by the isolation of iron(II) cyclometallated species combined with Mößbauer spectroscopic studies and stoichiometric experiments (Scheme 1a).[60−62] Subsequently, a low-valent Fe(0)/Fe(II) manifold was proposed by Ackermann and co-workers for the $[Fe(PMe_3)_4]$-catalyzed hydroarylation of allenes (Scheme 1b).[58] The proposed mechanism was based on the isolation of a cyclometallated iron hydride complex, which was postulated to be a catalytically active on-cycle species. Subsequent in-depth kinetic, spectroscopic, and density functional theory (DFT) investigations provided further mechanistic support.

It is therefore evident that mechanistic understanding for efficient, byproduct-free iron-catalyzed C−H activations is in high demand. Thereby, to accelerate the rationalization of such reactions and facilitate the discovery of new iron-based reactivity, we have now extended our mechanistic investigations on the $[Fe(PMe_3)_4]$-catalyzed hydroarylation of allenes.[58] As a result, an unexpected iron alkoxide complex was isolated and fully characterized, further clarifying the mode of operation of iron-catalyzed hydroarylations. Consequently, a mechanism is now presented with the on-cycle intermediate being a transient *fac*-iron hydride complex in equilibrium with the *mer*-iron hydride previously proposed.[58] The novel iron(II) cyclometalated alkoxide complex isolated enabled efficient catalysis by providing direct access to the catalytic cycle through a fast equilibrium with the *fac*-iron hydride complex. Deactivation pathways, along with the formation of potentially catalytically active off-cycle paramagnetic species, have been considered, which in combination with electron paramagnetic resonance (EPR), stoichiometric experiments, and detailed DFT studies provide further insights into the mode of action of low-valent iron-catalyzed C−H activations.

Scheme 1. In-Depth Mechanistically Explored Iron-Catalyzed C−H Activation Systems: (a) Iron-Catalyzed C−H Arylation, Alkylation, and Allylation of Aromatic Amides with Bidentate Directing Groups. (b) Additive-Free Hydroarylation of Allenes with Weak *O*-Carbonyl Chelation

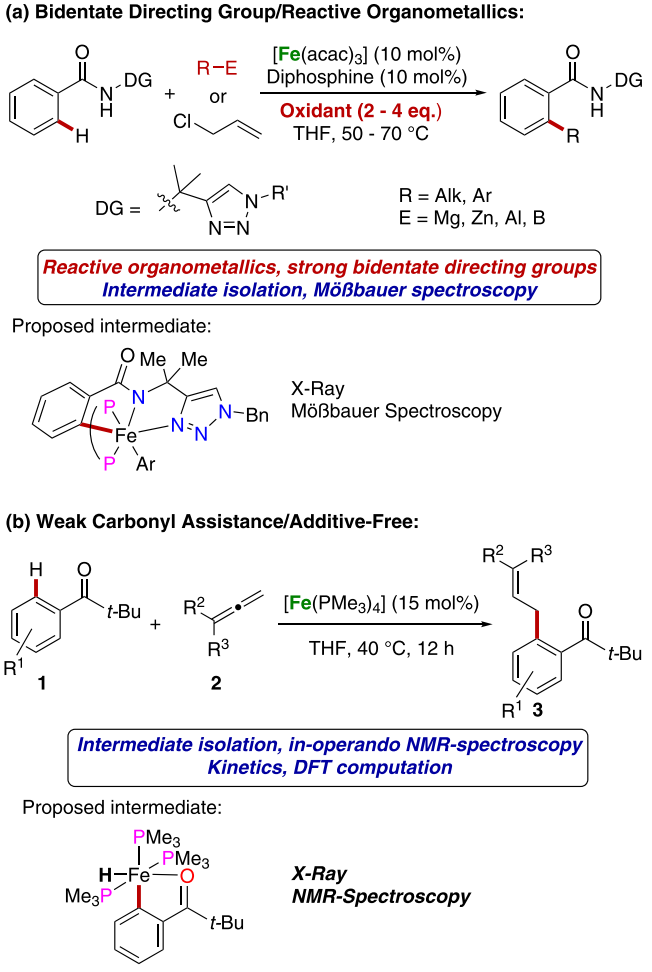

RESULTS AND DISCUSSION

Single crystals of the cyclometallated iron hydride complex **5** were previously obtained from the reaction between pivalophenone **1** and $[Fe(PMe_3)_4]$ (**4**) in toluene under partial vacuum to facilitate the removal of the trimethylphosphine (Figure 1).[58] However, several attempts to isolate a pure sample of **5** from toluene in high yield were unsuccessful. Therefore, the reaction between **1** and iron hydride **4** was conducted by dissolving the latter in two equivalents of ketone **1** under solvent-free conditions. Surprisingly, recrystallization of the obtained dark solid from pentane resulted in the isolation of turquoise crystals of the iron(II) alkoxide complex **6** instead of the expected iron hydride **5**, according to an X-ray crystallographic analysis (Figure 1). Complex **6** exhibits a characteristic singlet resonance at 3.90 ppm in its ^{1}H NMR spectrum for the benzoic methine hydrogen. In addition, no hydrogen gas was detected when the reaction between pivalophenone **1** and complex **4** was performed in a sealed vial, according to a headspace chromatographic analysis (Section S2.2 in the Supporting Information, SI). Pivalophenone **1** was selected as the standard substrate to avoid enolization at this point and because of its characteristic ^{1}H NMR spectroscopic *tert*-butyl resonance.

The reaction between **1** and **4** in a concentrated benzene solution (3.7 M in **4**) for 14 h followed by extraction with ether and recrystallization at −20 °C yielded the iron(II) hydride **5** in 52% yield, pointing toward the presence of an equilibrium between the two C−H activated iron species. This was further confirmed by studying the kinetic profile of a solution of iron(II) alkoxide **6** in C_6D_6 by ^{1}H NMR spectroscopy, revealing the formation of **5** accompanied by the formation of **4** (Figure 2, top), with the latter suggesting a reversible C−H activation step. Similarly, when hydride **5** was dissolved in C_6D_6, formation of alkoxide **6** occurred (Figure 2, bottom). This equilibrium is established through a reversible β-hydride elimination reaction in **6**, as supported by DFT calculations (*vide infra*). In addition, when hydride **5** was reacted with $[D]_5$-**6** in benzene, crossover products were not observed (compounds **A**−**D** in Scheme 2), demonstrating the purely intramolecular nature of this equilibrium (see also Section S3.6 in the Supporting Information).

Interestingly, a loss in mass balance was also observed when either **5** or **6** is dissolved in C_6D_6 as is evident by the negative slope of the reaction profile after equilibrium is established (Figure 2). This is attributed to the continuous formation of paramagnetic iron species from **5** or **6** in

https://doi.org/10.1021/acscatal.2c00772
ACS Catal. 2022, 12, 4947−4960

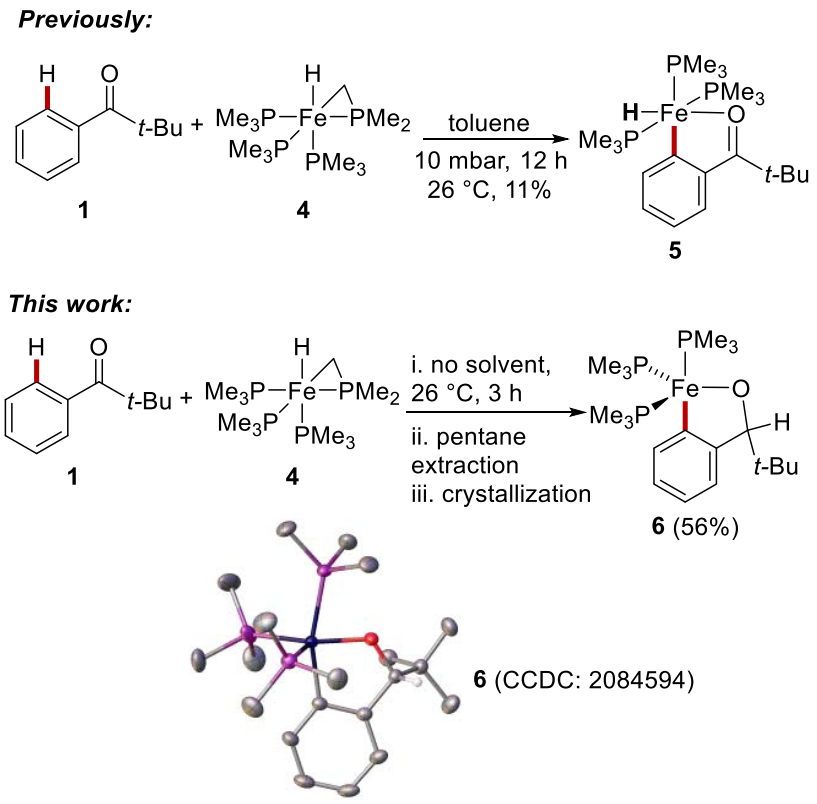

Figure 1. Synthesis of iron(II) alkoxides **5** and **6** and molecular structure of the latter. Thermal ellipsoids are drawn at the 50% probability level.

solution and is also supported by the presence of paramagnetic resonances in the ^{1}H NMR spectra (Figures S5 and S10). Therefore, to obtain further insight into the nature of these species, the reactions presented in Figure 2 were also monitored by EPR spectroscopy. Indeed, two signals were observed in the frozen solution EPR spectra of **5** and **6** over time: a sharp signal at 3350 G steadily increasing in intensity and a broad one at 3200 G, initially increasing and subsequently stabilizing (Sections S3.2 and S3.5 in the Supporting Information). The former signal shows *g*-values in the range of g_x = 2.17, g_y = 2.05, g_z = 2.00, with the hyperfine splitting of ^{31}P being a triplet resulting from coupling with 2 nuclei of I = 1/2 (e.g., two PMe_3 ligands) with A_{iso} = 26.41 G and the main intensity localized at around g = 2.00. These findings are in accordance with S = 1/2 compounds with one or more P-containing ligands with resolved hyperfine splittings.[63,64] Two paramagnetic compounds were also observed in the ^{1}H NMR spectra as broad resonances at high frequencies (Figures S5 and S10). Remarkably, an induction period was observed for the formation of these paramagnetic species when solutions of iron hydride **5** were measured by ^{1}H NMR spectroscopy in contrast to when alkoxide **6** was employed. This suggests that the paramagnetic compounds are formed from **6** rather than **5**, in line with the coordinative unsaturation and increased reactivity of **6** (*vide infra*). Several attempts to obtain single crystals of the paramagnetic species formed were unsuccessful. Similarly, LIFDI mass spectroscopy revealed only the presence of **5** and **6** in solution, while an electrospray ionization high-resolution mass spectrometry (ESI-HRMS) study of the reaction provided limited insight into the nature of the paramagnetic species formed (Section S3.3 in the Supporting Information).

When solutions of complex **4** and excess arene were reacted for extended periods of time (>12 h), formation of bridged iron(II) alkoxide complexes occurred (Figure 3). Single crystals of these species were isolated, but it was not possible to obtain analytically pure samples due to the complexity of the resulting reaction mixture.[65] The formation of the well-defined complexes **7** and **8** as well as the unidentified paramagnetic complexes are most likely related to catalyst deactivation pathways in the iron-catalyzed C−H activations of aryl ketones, which translated into the need for high iron loadings of up to 15 mol %.[56−58] It is noteworthy that similar observations have been reported by Beck and coworkers for the reaction between **4** or $[Co(PMe_3)_4]$ with benzophenone.[66]

Subsequently, the catalytic efficacy of the new iron alkoxide **6** was compared to the ones of iron(II) hydrides **4** and **5**. For this purpose, the iron-catalyzed hydroarylation of allene **2** with ketone **1** was performed using catalysts **4**, **5**, and **6** under otherwise identical reaction conditions.

All three reactions were monitored using *in operando* ^{1}H NMR spectroscopy (Figure 4, top). Notably, an extended induction period was observed in the kinetic profile of the reaction catalyzed by precatalyst **4**.[58] Surprisingly, the cyclometallated iron(II) hydride **5** also exhibited a significant induction period, albeit shorter compared to the one observed with the precatalyst **4**. The mere presence of an induction period excludes it from being on-cycle.[67,68] In sharp contrast, when the new iron(II) alkoxide **6** was employed, a considerably faster reaction was observed, with a complete absence of an induction period even when catalysis was performed at 7 °C (Figures 4 and S29), suggesting that the C−H activated complex **6** could be an intermediate in this iron-catalyzed hydroarylation. This is also supported by a

https://doi.org/10.1021/acscatal.2c00772
ACS Catal. 2022, 12, 4947−4960

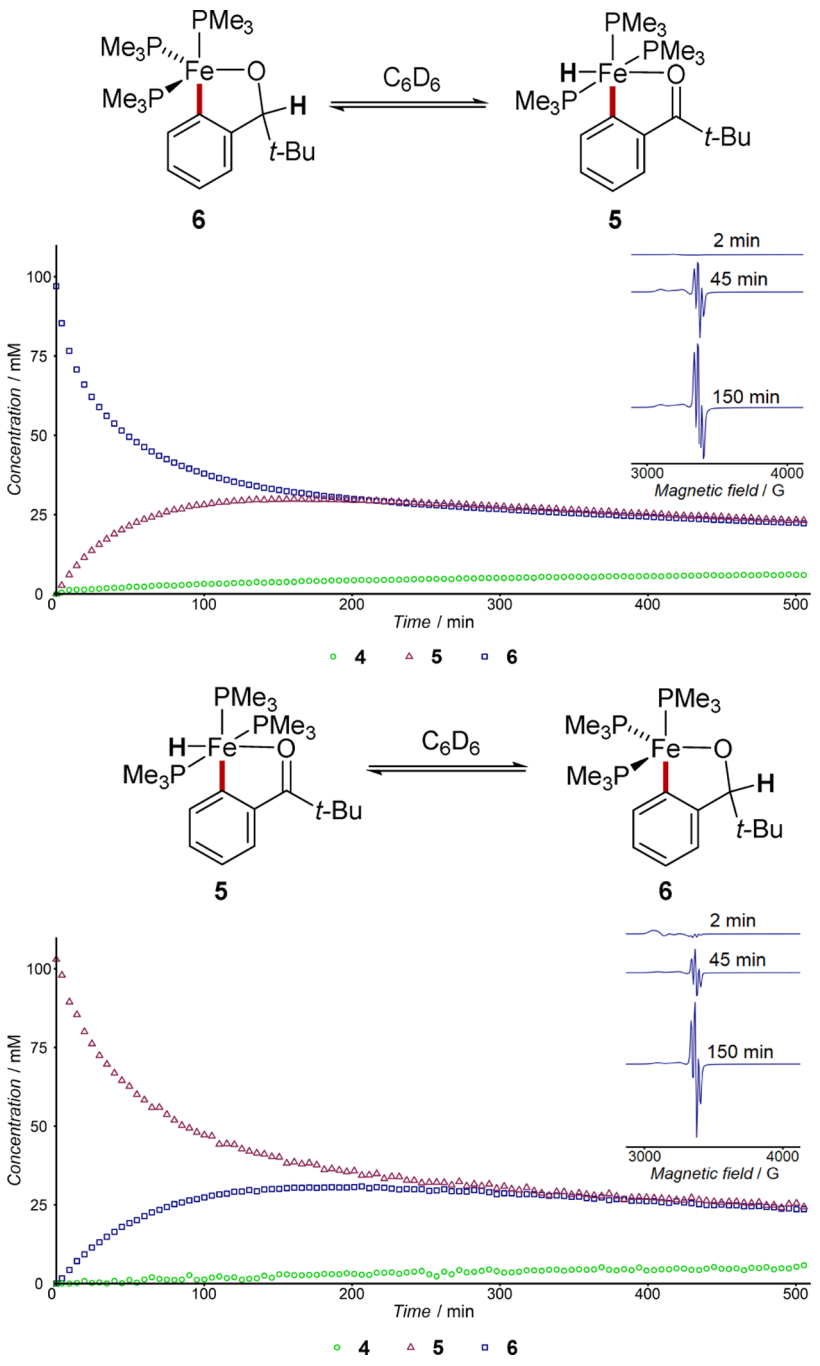

Figure 2. ^{1}H NMR (400 MHz, C_6D_6, 35 °C) and EPR (C_6D_6, 140 K) spectroscopic monitoring of a solution of **6** (97 mM in C_6D_6, top) and **5** (103 mM in C_6D_6, bottom) at 35 °C over time.

stoichiometric reaction between **2** and **6**, where an exceptionally high reaction rate was observed (reaction competed in only 20 min), again with a complete lack of any induction period (Figure S43). Lastly, similar to complex **4** and in line with our previous work,[58] a kinetic isotope effect of 1.0 was observed when an equimolar mixture of **6** and $[D]_5$-**6** at 10 mol % loading was used to catalyze the reaction between allene **2** and an equimolar mixture of **1** and $[D]_5$-**1** (Figure S24).

According to the experimental data presented so far, complex **6** is the strongest candidate for the role of the catalytically active intermediate in iron-catalyzed C−H activations by weak *O*-carbonyl chelation. However, when pure **6** is dissolved in benzene, formation of **4** and **5** is accompanied by two unidentified paramagnetic species which could be catalytically competent. To test this, the catalytic reaction was repeated with **6**, as described in Figure 4 and was this time monitored by EPR spectroscopy. The paramagnetic species observed in the equilibrium experiments (Figure 2) are also observed during catalysis. However, their increase in concentration at 60 min succeeds catalysis, suggesting that they are more likely to be related to catalyst deactivation processes. To further rule out such paramagnetic products from being catalytically active, the catalytic reaction was repeated at 25 °C, being activated with a fresh solution of **6** in C_6D_6. This resulted in a more detailed profile, where

https://doi.org/10.1021/acscatal.2c00772
ACS Catal. 2022, 12, 4947−4960

Scheme 2. Crossover Experiment between Iron Hydride 5 and Deuterium Labeled $[D]_5$-6

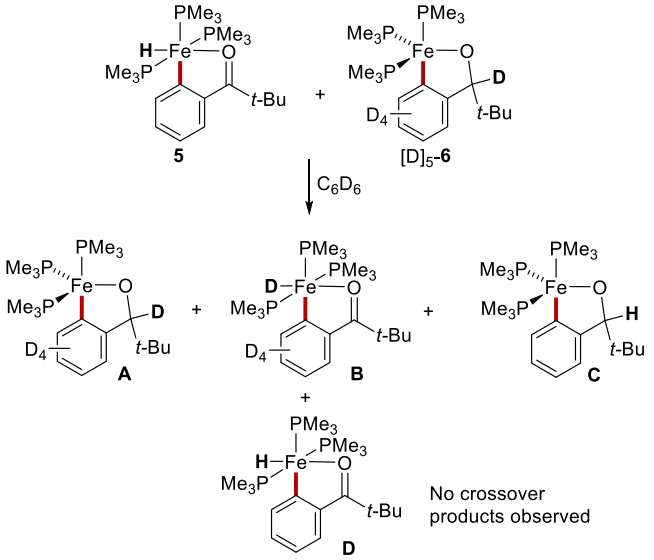

the change of the concentration of **6** can be monitored throughout catalysis, followed by subsequent formation of **5** toward the end of the catalytic activity (Figure 5). Subsequently, the reaction was repeated using the same solution of **6** after it was incubated at 35 °C for 500 min under otherwise identical conditions (Figure 5, red stars). Judging from the reduced catalytic activity of the incubated (and therefore enriched in paramagnetic species) solution of **6**, it can be concluded that the paramagnetic species formed are not catalytically active.

Upon closer inspection of the nascent stages of catalysis in Figure 5, it becomes apparent that a high concentration of **6** in solution is accompanied by high catalytic activity, while the concentration of **5** increases toward the end of the catalytic activity, further demonstrating the catalytic superiority of **6** against **5**. A similar situation is observed when complex **5** is used to initiate catalysis, where during the induction period, an increased concentration of **5** is observed, with **6** being essentially absent (Figure S22). As the concentration of **6** increases, so does the production of **3**.

The high catalytic performance as well as reactivity observed for ferracycle **6** stems from the lability of the trimethylphosphine ligands, which leads to the formation of coordinatively unsaturated intermediates suitable for binding the olefinic substrate.[69] Alternatively, the coordinative unsaturation of metallacycle **6** could facilitate its conversion to an even more active species that mediates catalysis. The intimate relationship between phosphine lability and catalytic activity can be further demonstrated from the reaction between **5** or **6** with the bidentate equivalent of PMe_3, namely 1,2-bis(dimethylphosphino)ethane (dmpe), toward formation of alkoxide **9** (Figure 6). Hence, complex **9**, despite being an iron(II) alkoxide similar to **6**, was found to be inert toward allene **2**, with no reaction observed according to an ^{1}H NMR spectroscopic analysis of an equimolar solution of **2** and **9** in C_6D_6. A similar effect has also recently been reported, where the use of strongly chelating diphosphine ligands leads to reduced reaction rates in iron-catalyzed C–H allylations.[61] This striking difference between iron(II) alkoxides **6** and **9** is attributed to the increased coordination strength of dmpe in the latter complex. Likewise, these findings emphasize the importance of choosing the appropriate phosphine for the development of

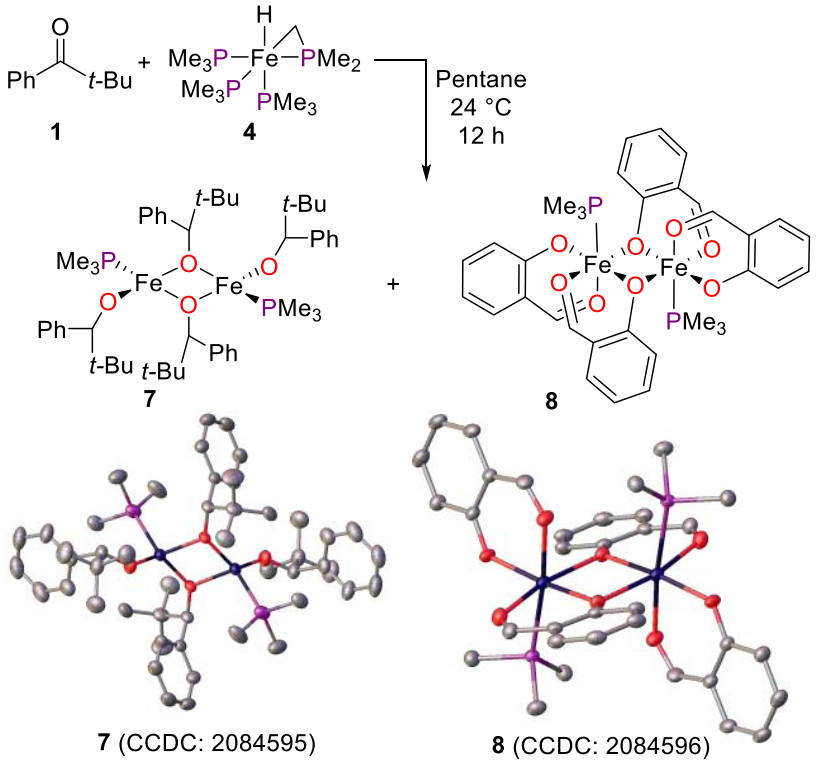

Figure 3. Isolation and molecular structures of complexes **7** and **8**. Thermal ellipsoids are drawn at the 50% probability level, and H atoms are omitted for clarity.

https://doi.org/10.1021/acscatal.2c00772
ACS Catal. 2022, 12, 4947–4960

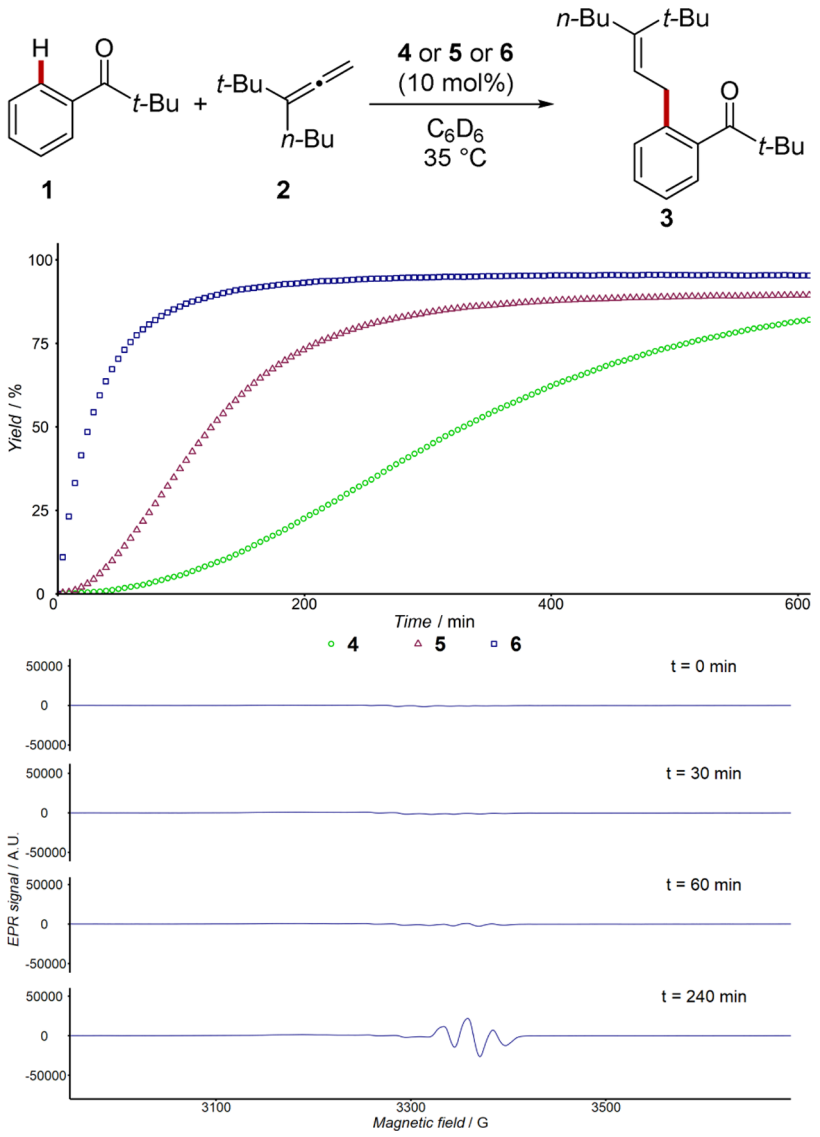

Figure 4. ^{1}H NMR (400 MHz, C_6D_6, 35 °C, top) spectroscopic monitoring of the reaction between pivalophenone **1** and allene **2** with precatalysts **4** (green circle), **5** (red triangle), and **6** (navy square) at 10 mol % loading, and EPR (C_6D_6, 140 K, bottom) spectroscopic monitoring of the reaction between pivalophenone **1** and allene **2** with precatalyst **6**.

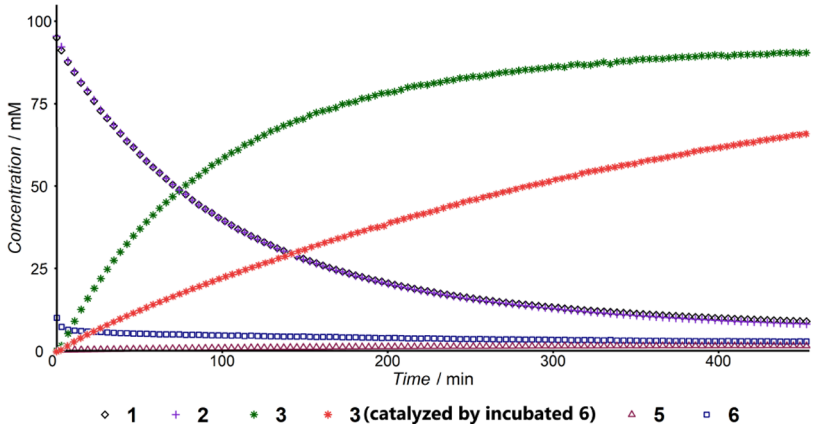

Figure 5. ^{1}H NMR (400 MHz, C_6D_6, 25 °C) spectroscopic monitoring of the reaction between pivalophenone **1** (black rhombe) and allene **2** (purple cross) catalyzed by either a fresh solution of **6** (navy square) at 10 mol % to form **3** (green stars) with subsequent generation of **5** (red triangle) or by a solution of **6**, which was kept at 35 °C for 500 min at 10 mol % to form **3** (red stars) at a reduced rate (see also Figures S25–S28).

https://doi.org/10.1021/acscatal.2c00772
ACS Catal. 2022, 12, 4947−4960

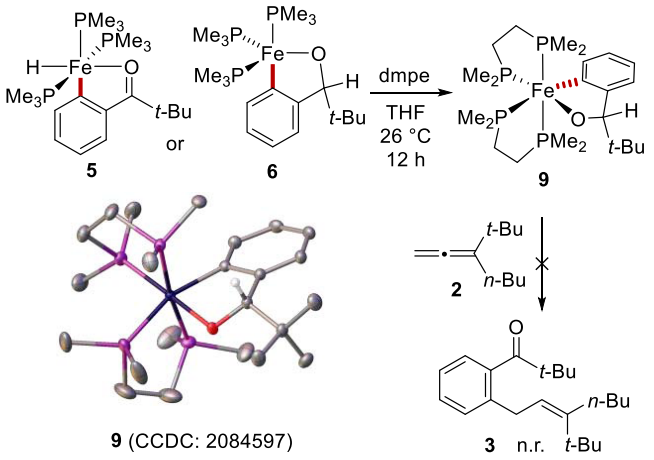

Figure 6. Synthesis of iron(II) alkoxide **9** and reaction with allene **2**. Note that **9** was isolated as a mixture of stereoisomers with the major isomer (90%) presented here.

iron-catalyzed C−H activations by weak chelation-assistance.[56−59] In this context, it is noteworthy that C−H activation with *N*-heterocyclic carbene (NHC) ligands is viable,[70] including an enantioselective transformation by low-valent iron catalysis.[47]

The crucial question is related to the mechanism by which iron(II) alkoxide **6** is formed upon reaction of arene **1** with iron(II) tetraphosphine complex **4**. Typically, such transformations were proposed to proceed *via* an oxidative addition to a low-valent iron complex.[56−59,66,71,72] However, for the oxidative addition pathway to be viable, two requirements need to be met. First, the formation of a low-valent iron species, and second, the formation of a hydride complex prior to the formation of alkoxide **6** (Scheme 3). According to previous reports and NMR spectroscopic analyses, complex **4** is in fact an iron(II) hydride in solution without any trace of $[Fe(PMe_3)_4]$ being observed in any spectroscopic data reported so far.[73] Additionally, hydride complex **4** was found to be a rather weak acid considering its high pK_a^{THF} value of 55.8 with a pK_a^{THF} of 20 for the conjugate acid of $[Fe(PMe_3)_4]$.[74] It has therefore been previously proposed that the iron(0) $[Fe(PMe_3)_4]$ form exists in undetectable trace amounts in equilibrium with the iron(II) form (complex **4**) and therefore oxidative addition becomes possible.[56−59,66,71,72,75] To further probe the hypothesis that complex **4** can obtain an iron(0) form, a reaction of the latter with a strongly coordinating dmpe ligand was performed. Indeed, addition of two equivalents of dmpe in a solution of **4** resulted in the formation of the previously reported iron(0) complex $[Fe(PMe_3)(dmpe)_2]$ (**10**) (Supporting Information; Section S2.4).[76] Hence, a low-valent iron species is accessible from the iron(II) hydride complex **4**, which is in line with the working hypothesis presented in Scheme 3.

The second requirement for an oxidative addition mechanism to be operative is that an iron hydride complex must form before the generation of **6**. Subsequent nucleophilic attack of the hydride to the carbonyl in the hydride complex formed should generate **6**. To probe this hypothesis, the reaction between arene **1** and precatalyst **4** was monitored by ^1H and ^{31}P NMR spectroscopy (Figure 7). Immediate formation of complex **6** was observed while the concentration of iron hydride **5** started rising only after a significant amount of iron alkoxide **6** had formed, resulting in an induction period. Therefore, complex **6** forms prior to complex **5**, excluding the latter from being the on-cycle hydride complex of interest. It must be noted that no significant amounts of other iron-containing species are generated during this reaction according to the good mass balance observed (Figure 7, gray crosses). Subsequently, the same reaction between **1** and **4** was monitored by ^{31}P NMR spectroscopy, this time replacing **1** with $[D]_5$-**1** under otherwise identical conditions (Figure 7, bottom). No kinetic isotope effect was observed for the consumption of pivalophenone **1** (k_H/k_D = 1.0) in support of a facile oxidative addition step and a slow phosphine abstraction in line with our previously reported results.[58] As expected, an equilibrium isotope effect is also observed, with the $[D]_5$-**5**/$[D]_5$-**6** equilibrium being significantly shifted toward $[D]_5$-**6**.[77] Most importantly, a weak kinetic isotope effect for the formation of **6** (k_H/k_D = 1.3) was found, suggesting that an iron-hydrogen bond cleavage occurs prior to its formation.

Thus far, it has been demonstrated that precatalyst **4** is an iron hydride complex and that its reaction with **1** produces an iron alkoxide complex **6** from an iron hydride complex that cannot be **5**. At the same time, insertion of ketone **1** into iron hydrides is a well-established reaction and several iron-catalyzed ketone hydrogenations have been reported to operate *via* a carbonyl insertion to a metal hydride, followed by the formation of an iron alkoxide intermediate.[78−82]

Scheme 3. Hypothesized Mechanism for the C−H Activation of Aromatic Ketones Mediated by 4 *via* Oxidative Addition

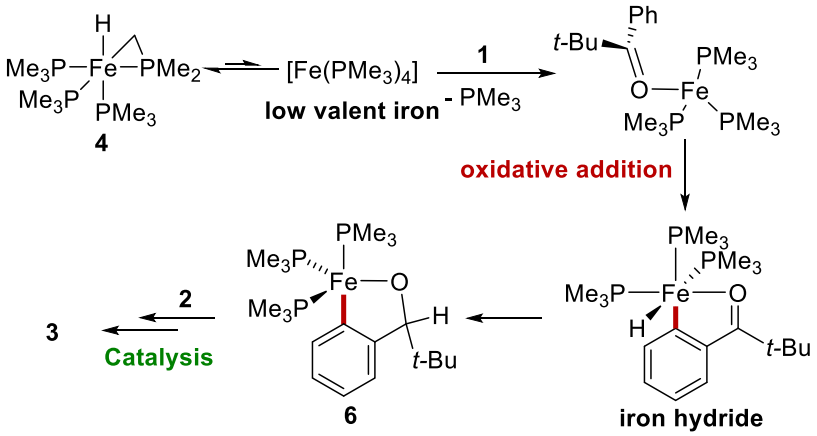

https://doi.org/10.1021/acscatal.2c00772
ACS Catal. 2022, 12, 4947−4960

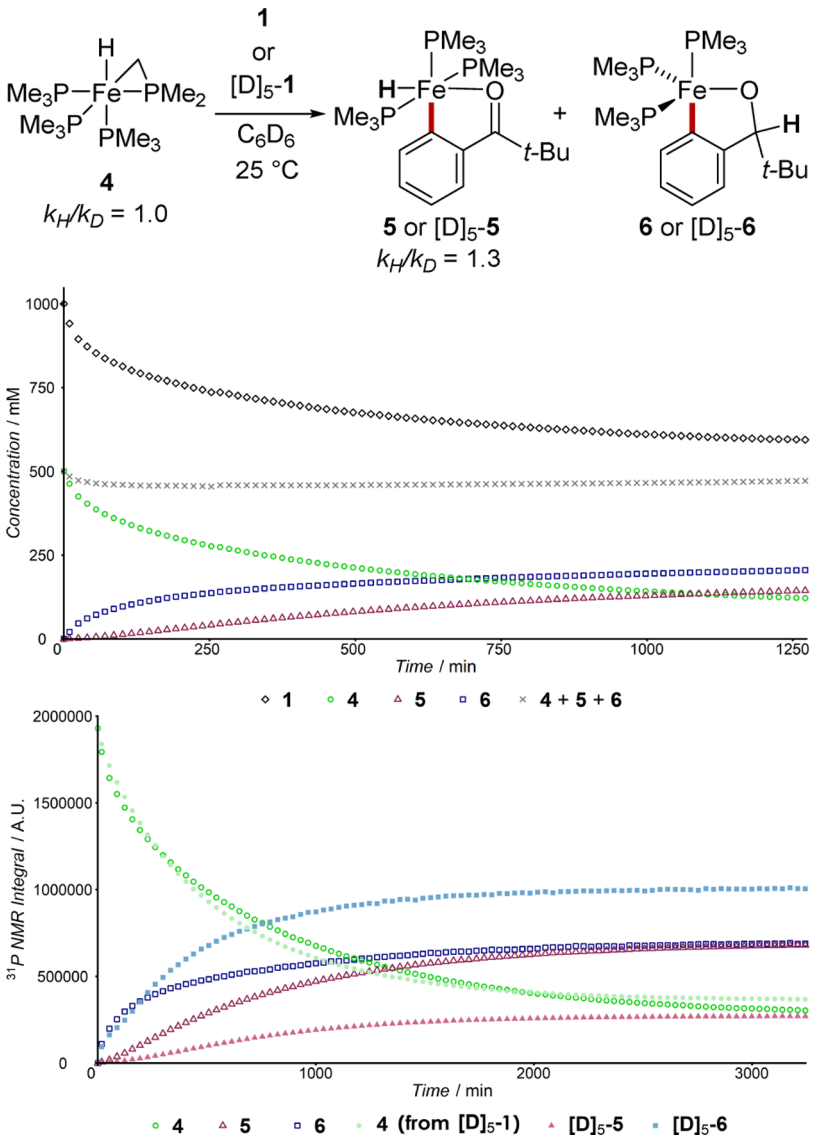

Figure 7. ^{1}H NMR (400 MHz, C_6D_6, 25 °C, top) spectroscopic monitoring of the reaction between arene **1** (1000 mM) and precatalyst **4** (500 mM) to form **5** and **6**. ^{31}P NMR (126 MHz, C_6D_6, 25 °C, bottom) spectroscopic monitoring of two independent reactions between precatalyst **4** (500 mM) and phenone **1** or $[D]_5$-**1** (1000 mM) to form **5** and **6** or $[D]_5$-**5** and $[D]_5$-**6**, respectively, with the overlayed plots presented here (Figures S30−S38).

Therefore, to differentiate between an oxidative addition pathway and a nucleophilic attack of the hydride to the carbonyl manifold, complex $[D]_5$-**6** was synthesized by reacting labeled $[D]_5$-**1** with precatalyst **4** (Scheme 4). According to the detailed ^{1}H and ^{2}H NMR spectroscopic analyses (Section S5.4 in the Supporting Information), quantitative deuteration of the *β*-alkoxy carbon was observed, which advocates against the nucleophilic attack of the hydride to the carbonyl scenario.

Based on our experimental evidence, we hypothesized whether the C−H activation of pivalophenone **1** by precatalyst **4** is initiated by a reductive elimination in the iron(II) complex **4** (**I-1** in Figure 8) to give the iron(0) complex $[Fe(PMe_3)_4]$ (**I-2**). Substitution of a PMe_3 by pivalophenone **1** followed by oxidative addition could lead to a transient *fac*-hydride complex **I-5**. Complex **I-5** would immediately react—and therefore cannot be observed spectroscopically or isolated—by nucleophilic attack of the hydride to the carbonyl, converting the weakly directing L-type carbonyl to a strongly coordinating X-type alkoxide group to form the isolated complex **6** (**I-6** in Figure 8). Indeed, the DFT calculated ^{1}H NMR chemical shift for **I-5** of −7.6 ppm could not be observed in any of the recorded ^{1}H NMR spectra even when the catalytic reaction was performed at −7 °C (*vide supra*). At the same time, but with a slower rate, complex **I-5** could isomerize to its *mer* isomer **5** (**I-7** in Figure 8).

At this point, two possibilities are envisioned for complex **6** in terms of its role in catalysis. It could either be an on-cycle intermediate resulting from a nucleophilic attack of the hydride to the carbonyl in **I-5**, or it could be off-cycle but in fast equilibrium with **I-5**, which then facilitates catalysis. To assess which is the most likely scenario, DFT calculations were carried out for the two main possible catalytic pathways at the TPSS-D4/def2-TZVP+SMD(Benzene)//TPSS-D3(BJ)/def2-SVP level of theory (Figure 8, and SI Section S7),[83−91] which was previously found to be optimal,[58] particularly for describing the spin states of the isolated

https://doi.org/10.1021/acscatal.2c00772
ACS Catal. 2022, 12, 4947−4960

Scheme 4. Synthesis of $[D]_5$-6 and Differentiation between Oxidative Addition and Nucleophilic Attack of the Hydride to the Carbonyl

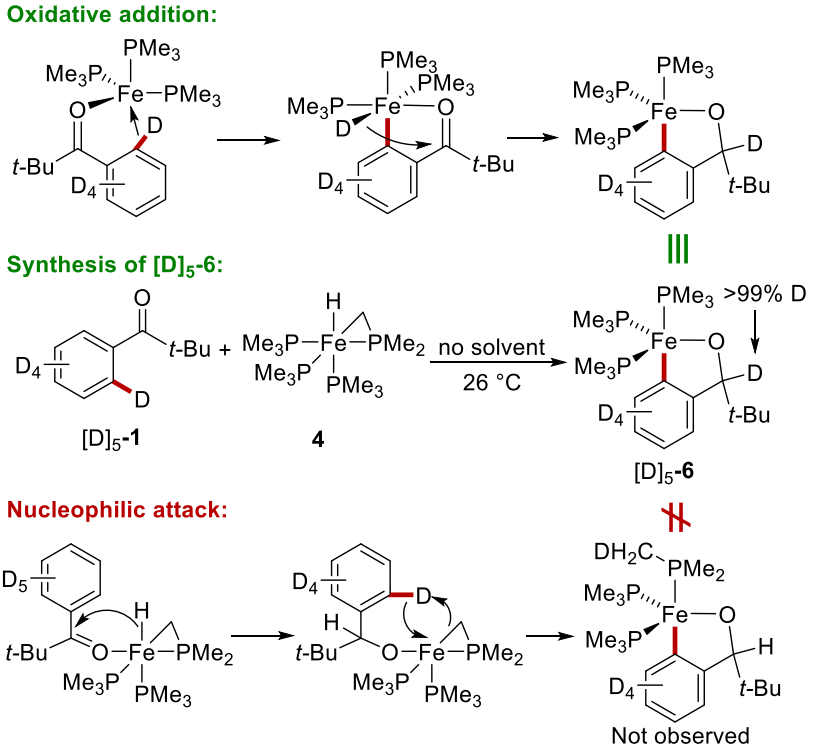

diamagnetic complexes **5** and **6**. Due to the electronic nature of the metal center, low-spin (singlet), high-spin (quintet), and intermediate-spin (triplet) complexes were considered in this study. The computational studies commenced from the iron hydride complex **I-1**, which undergoes reductive elimination to give the iron(0) complex **I-2** by spin-crossover with a barrier of 16.2 kcal mol^{-1}. Coordination of the ketone **1** followed by phosphine ligand dissociation leads to **I-4** on a singlet surface. Alternative mechanisms between complex **I-1** and **I-5** were also probed but were found energetically disfavored (Figures S49 and S50). Subsequently, C−H activation proceeds *via* a barrierless oxidative addition pathway, forming the thermodynamically more stable *fac*-iron(II) hydride complex **I-5**, which can be converted either to the iron(II) alkoxide species **I-6** or isomerize to its *mer*-hydride isomer **I-7**. The three species **I-5**, **I-6**, and **I-7** are in equilibrium, considering that they are energetically comparable within a difference of 3.1 kcal mol^{-1} on a singlet surface, which is in line with the experimental results presented in Figure 2. The formation of the iron(II) alkoxide **I-6** was kinetically most favorable, with a computed barrier of 15.0 kcal mol^{-1}. Therefore, the isomerization pathway is less favorable by 6.6 kcal mol^{-1}, which is in line with the experimentally observed formation of intermediate **6** prior to **5**. In the case where catalysis is mediated by **6** (Figure 8, alkoxide-catalyzed mechanism), decoordination of PMe_3 from iron(II) alkoxide **I-6** proved to be rate-determining, yielding a more endergonic complex **I-8** (by 17 kcal mol^{-1}), which undergoes isomerization through spin-crossover with a barrier of 10.3 kcal mol^{-1} to form complex **I-9** in a triplet state. After coordination of the allene (**I-10**), migratory insertion takes place by what can be considered a three-state reactivity, through a more favorable singlet surface (**TS(10−11)**) with a barrier of 7.9 kcal mol^{-1} to generate complex **I-11** in a quintet surface. The iron(II) complex **I-11** leads to the formation of iron(II) hydride complex **I-12** by β-H elimination with a barrier of 15 kcal mol^{-1}. Subsequently, **I-12** undergoes facile reductive elimination to form the final product, which is *O*-coordinated to the metal center by an agostic interaction in complex **I-13**. Similar results were obtained when the calculations were performed in tetrahydrofuran (THF) instead of benzene as the solvent (Figure S51). An alternative pathway involving a concerted oxidative addition/hydrometallation was also considered (Figures 8 and S52 for a dissociative mechanism). However, the dominant pathway was found to be the one presented in Figure 9, for which catalysis is initiated by the *cis*-iron hydride **I-5**. Thus, after dissociation of a phosphine, **I-5** generates $\mathbf{I\text{-}6^B}$, which incorporates the allene **2** to form $\mathbf{I\text{-}7^B}$. Since ligand rearrangement at $\mathbf{I\text{-}6^B}$ was found to be less favorable (Figure S53), a facile migratory insertion of the allene to the hydride in $\mathbf{I\text{-}7^B}$, followed by rearrangement of the ligands, results in metal intermediate $\mathbf{I\text{-}9^B}$. Finally, rate-determining reductive elimination yields the desired product **3** and regenerates the catalyst.

Taking the above together, the catalytic cycle presented in Scheme 5 is proposed. The cycle commences by a reductive elimination in complex **4** to establish an equilibrium with the iron(0) complex **I-2**. Coordination of **1** follows to form **I-3**, which facilitates phosphine decoordination, leading to **I-4**. Reversible facile C−H activation via oxidative addition leads to the bifurcation point in the cycle, the *fac*-iron hydride **I-5**, which can either isomerize to form the previously isolated mer-iron hydride isomer **5** or undergo nucleophilic attack of the hydride to the carbonyl toward the formation of **6**. Both **5** and **6** can potentially transform to catalytically inactive complexes accompanied by cessation of the catalytic activity. Phosphine decoordination from *fac*-iron hydride **I-5** followed

https://doi.org/10.1021/acscatal.2c00772
ACS Catal. 2022, 12, 4947−4960

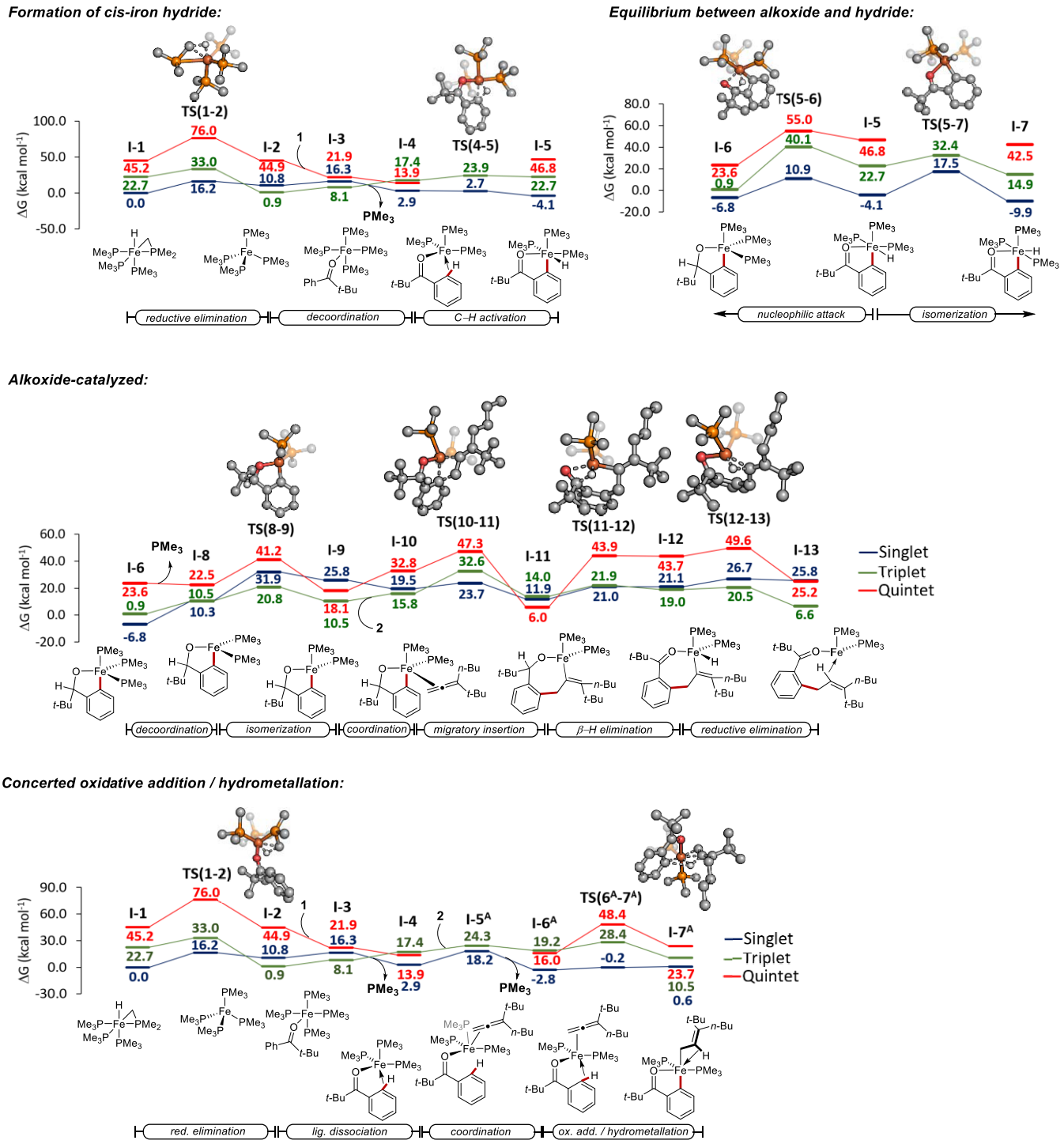

Figure 8. Alternative pathways. Computed relative Gibbs free energies ($\Delta G_{308.15}$) in kcal mol^{-1} at the TPSS-D4/def2-TZVP+SMD(Benzene)//TPSS-D3(BJ)/def2-SVP level of theory. Energy values are given with respect to **I-1**. In the computed transition state structures, nonrelevant hydrogen atoms were omitted for clarity.

by allene coordination can lead to intermediate **I-7**$^{\mathbf{B}}$, which then undergoes migratory insertion and reductive elimination to yield **I-10**$^{\mathbf{B}}$. The proposed mechanism is not only in line with the experimental results presented in Figure 7 and Scheme 4, where formation of **6** precedes that of **5** and full deuteration at the benzylic carbon position was observed in [D]$_5$-**6** but also with the previously observed reduced catalytic activity upon addition of PMe_3 during catalysis.[58]

CONCLUSIONS

In summary, we have performed detailed mechanistic studies on [Fe(PMe_3)$_4$]-catalyzed C−H activations, where an unanticipated five-coordinated iron(II) alkoxide complex was isolated and fully characterized. Subsequent experimentation revealed a mechanistically intricate system involving several equilibria in which the isolated alkoxide complex reversibly converts to a *mer*-hydride through its *fac* counterpart. At the same time, both complexes slowly

https://doi.org/10.1021/acscatal.2c00772
ACS Catal. 2022, 12, 4947−4960

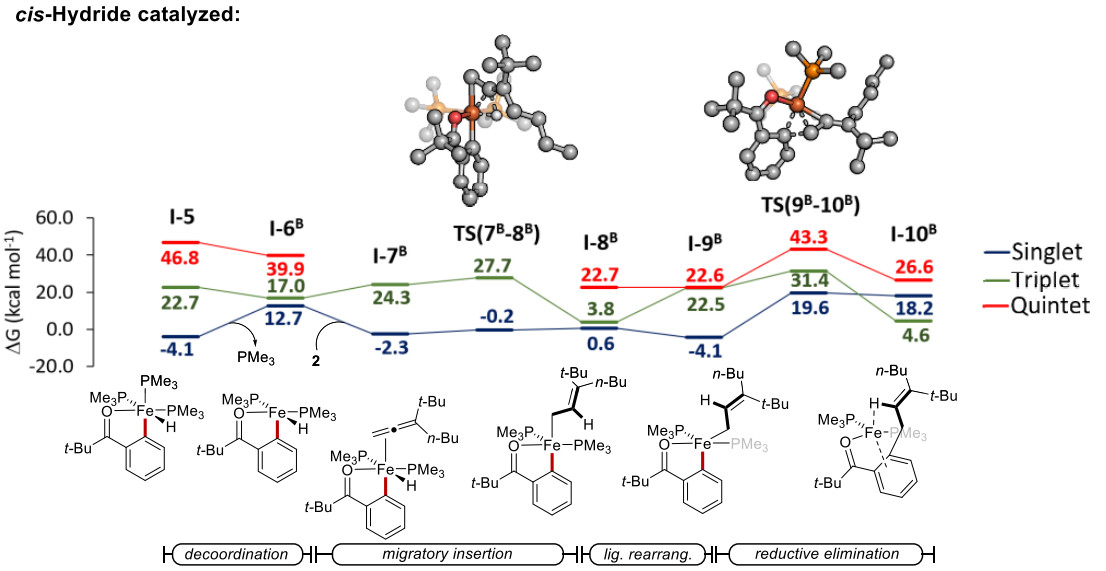

Figure 9. Favored mechanism *via cis*-hydride **I-5**. Computed relative Gibbs free energies ($\Delta G_{308.15}$) in kcal mol^{-1} at the TPSS-D4/def2-TZVP +SMD(Benzene)//TPSS-D3(BJ)/def2-SVP level of theory. Energy values are given with respect to **I-1**. In the computed transition state structures, nonrelevant hydrogen atoms were omitted for clarity.

Scheme 5. Proposed Mechanism for the C−H Activation of Aromatic Ketones Mediated by 4[a]

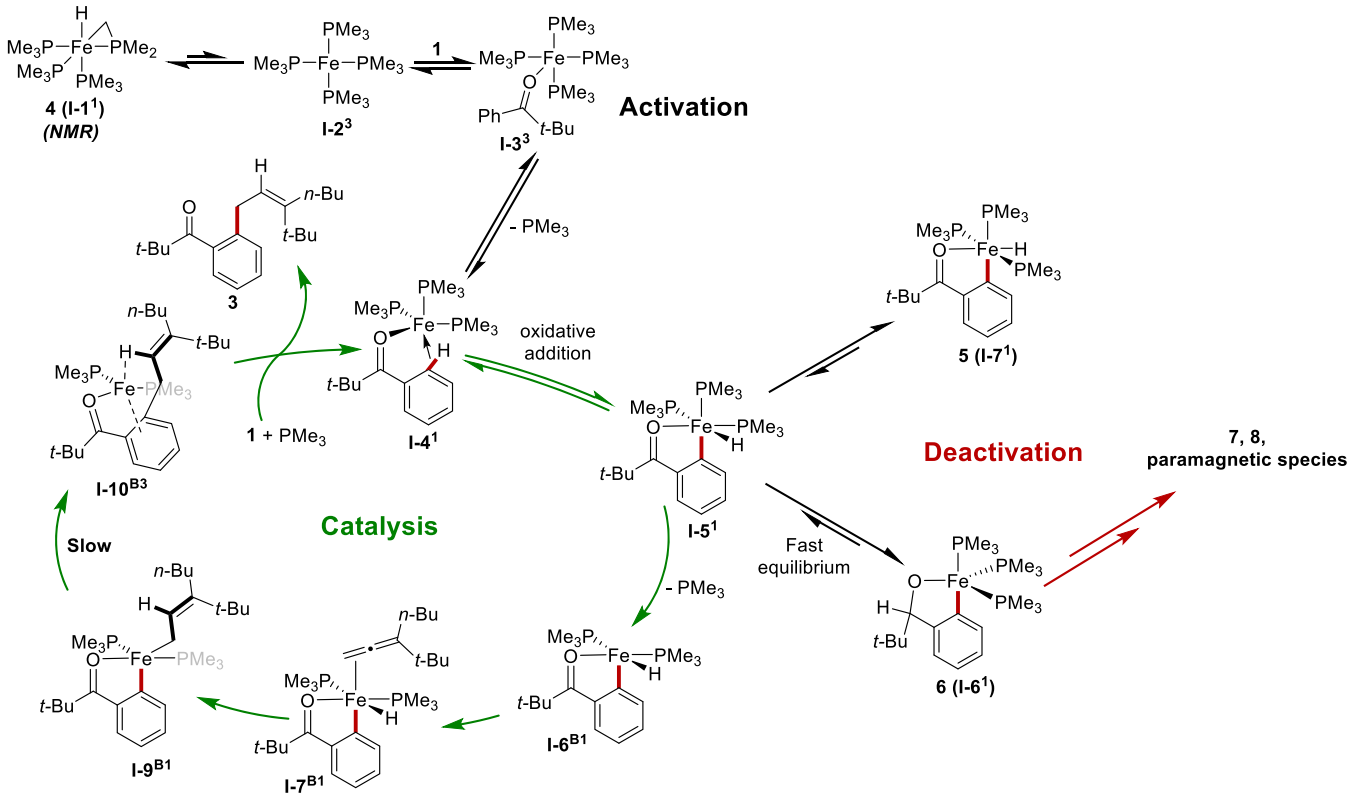

[a]Superscript numbers correspond to the most stable spin state.

decompose toward the formation of paramagnetic species, which were excluded from being catalytically active. Similarly, while the *mer*-hydride was unequivocally excluded from being on-cycle, isolation of the *fac*-hydride, being a transient intermediate, was not possible. Therefore, to distinguish between two possible mechanistic scenarios where the alkoxide is either an on-cycle species or an off-cycle resting state in fast equilibrium with the *fac*-hydride iron complex, detailed DFT calculations were performed. According to these computational studies, both pathways are plausible, with the latter pathway being computationally favored. We believe that the identification of novel cyclometallated iron alkoxide complexes in Grignard-free iron-catalyzed C−H activations should prove instrumental for further developments in this emerging area, for instance, toward stereoselective low-valent iron-catalyzed C−H activations.

https://doi.org/10.1021/acscatal.2c00772
ACS Catal. 2022, 12, 4947−4960

■ ASSOCIATED CONTENT

Supporting Information

The Supporting Information is available free of charge at https://pubs.acs.org/doi/10.1021/acscatal.2c00772.

Experimental procedures, compound characterization data, kinetic analyses, X-ray crystal details, and computational studies; X-ray crystallographic data for **4**−**8** (PDF)

■ AUTHOR INFORMATION

Corresponding Author

Lutz Ackermann − *Institut für Organische und Biomolekulare Chemie, Georg-August-Universität Göttingen, 37077 Göttingen, Germany; Wöhler-Research Institute for Sustainable Chemistry (WISCh), Georg-August-Universität Göttingen, 37077 Göttingen, Germany;* orcid.org/0000-0001-7034-8772; Email: Lutz.Ackermann@chemie.uni-goettingen.de

Authors

Antonis M. Messinis − *Institut für Organische und Biomolekulare Chemie, Georg-August-Universität Göttingen, 37077 Göttingen, Germany*

João C. A. Oliveira − *Institut für Organische und Biomolekulare Chemie, Georg-August-Universität Göttingen, 37077 Göttingen, Germany*

A. Claudia Stückl − *Institut für Anorganische Chemie, Georg-August-Universität Göttingen, 37077 Göttingen, Germany*

Complete contact information is available at: https://pubs.acs.org/10.1021/acscatal.2c00772

Author Contributions

A.M.M. performed experiments, synthesized complexes, and performed kinetic analyses. J.C.A.O. performed computational studies. A.C.S. performed EPR studies. L.A. supervised the project. A.M.M., J.C.A.O., and L.A. wrote the manuscript.

Notes

The authors declare no competing financial interest.

■ ACKNOWLEDGMENTS

Generous support by the DFG (SPP 1807 Gottfried-Wilhelm-Leibniz Award to LA) and the European Union's Horizon 2020 research and innovation programme (Marie Skłodowska-Curie Grant Agreement No. 895404 to A.M.M. and ERC advanced Grant to L.A.) is gratefully acknowledged. The authors thank Dr. Christopher Golz (Göttingen University) for assistance with the X-ray diffraction analysis, Dr. Lianrui Hu for preliminary computational studies, and Dr. Michael John for help with NMR studies.

■ REFERENCES

(1) Park, Y.; Kim, Y.; Chang, S. Transition Metal-Catalyzed C−H Amination: Scope, Mechanism, and Applications. *Chem. Rev.* **2017**, *117*, 9247−9301.

(2) Davies, H. M. L.; Morton, D. Collective Approach to Advancing C−H Functionalization. *ACS Cent. Sci.* **2017**, *3*, 936−943.

(3) Lyons, T. W.; Sanford, M. S. Palladium-Catalyzed Ligand-Directed C−H Functionalization Reactions. *Chem. Rev.* **2010**, *110*, 1147−1169.

(4) Leitch, J. A.; Frost, C. G. Ruthenium-Catalysed σ-Activation for Remote *Meta*-Selective C−H Functionalisation. *Chem. Soc. Rev.* **2017**, *46*, 7145−7153.

(5) Gensch, T.; Hopkinson, M. N.; Glorius, F.; Wencel-Delord, J. Mild Metal-Catalyzed C−H Activation: Examples and Concepts. *Chem. Soc. Rev.* **2016**, *45*, 2900−2936.

(6) Rej, S.; Ano, Y.; Chatani, N. Bidentate Directing Groups: An Efficient Tool in C−H Bond Functionalization Chemistry for the Expedient Construction of C−C Bonds. *Chem. Rev.* **2020**, *120*, 1788−1887.

(7) Sun, C.-L.; Li, B.-J.; Shi, Z.-J. Direct C−H Transformation via Iron Catalysis. *Chem. Rev.* **2011**, *111*, 1293−1314.

(8) He, J.; Wasa, M.; Chan, K. S. L.; Shao, Q.; Yu, J.-Q. Palladium-Catalyzed Transformations of Alkyl C−H Bonds. *Chem. Rev.* **2017**, *117*, 8754−8786.

(9) Arockiam, P. B.; Bruneau, C.; Dixneuf, P. H. Ruthenium(II)-Catalyzed C−H Bond Activation and Functionalization. *Chem. Rev.* **2012**, *112*, 5879−5918.

(10) Colby, D. A.; Tsai, A. S.; Bergman, R. G.; Ellman, J. A. Rhodium Catalyzed Chelation-Assisted C−H Bond Functionalization Reactions. *Acc. Chem. Res.* **2012**, *45*, 814−825.

(11) Ackermann, L. Carboxylate-Assisted Transition-Metal-Catalyzed C−H Bond Functionalizations: Mechanism and Scope. *Chem. Rev.* **2011**, *111*, 1315−1345.

(12) Dyker, G. *Handbook of C−H Transformations: Applications in Organic Synthesis*; Wiley-VCH Verlag GmbH & Co. KGaA: Weinheim, 2005.

(13) Dixneuf, P. H.; Doucet, H. *Topics in Organometallic Chemistry: C−H Bond Activation and Catalytic Functionalization*; Springer: Heidelberg, 2016.

(14) Catalytic Transformations via C−H Activation. In *Science of Synthesis*; Yu, J.-Q., Ed.; Thieme: Stuttgart, 2016; Vol. *1*−*2*.

(15) Hartwig, J. F. Evolution of C−H Bond Functionalization from Methane to Methodology. *J. Am. Chem. Soc.* **2016**, *138*, 2−24.

(16) Rej, S.; Das, A.; Chatani, N. Strategic evolution in transition metal-catalyzed directed C−H bond activation and future directions. *Coord. Chem. Rev.* **2021**, *431*, No. 213683.

(17) Sarpong, R. C−H Functionalization/Activation in Organic Synthesis. *Beilstein J. Org. Chem.* **2016**, *12*, 2315−2316.

(18) Yang, Y.; Lan, J.; You, J. Oxidative C−H/C−H Coupling Reactions between Two (Hetero)arenes. *Chem. Rev.* **2017**, *117*, 8787−8863.

(19) McMurray, L.; O'Hara, F.; Gaunt, M. J. Recent Developments in Natural Product Synthesis Using Metal-Catalysed C−H bond Functionalisation. *Chem. Soc. Rev.* **2011**, *40*, 1885−1898.

(20) Segawa, Y.; Maekawa, T.; Itami, K. Synthesis of Extended π-Systems through C−H Activation. *Angew. Chem., Int. Ed.* **2015**, *54*, 66−81.

(21) Stepek, I. A.; Itami, K. Recent Advances in C−H Activation for the Synthesis of π-Extended Materials. *ACS Mater. Lett.* **2020**, *2*, 951−974.

(22) Seki, M. A New Catalytic System for Ru-Catalyzed C−H Arylation Reactions and Its Application in the Practical Syntheses of Pharmaceutical Agents. *Org. Process Res. Dev.* **2016**, *20*, 867−877.

(23) Çapcı, A.; Lorion, M. M.; Mai, C.; Hahn, F.; Hodek, J.; Wangen, C.; Weber, J.; Marschall, M.; Ackermann, L.; Tsogoeva, S. B. Cover Feature: (Iso)Quinoline−Artemisinin Hybrids Prepared through Click Chemistry: Highly Potent Agents against Viruses. *Chem. - Eur. J.* **2020**, *26*, No. 11912.

(24) Kaplaneris, N.; Kaltenhäuser, F.; Sirvinskaite, G.; Fan, S.; De Oliveira, T.; Conradi, L.-C.; Ackermann, L. Late-Stage Stitching Enabled by Manganese-Catalyzed C−H Activation: Peptide Ligation and Access to Cyclopeptides. *Sci. Adv.* **2021**, *7*, No. eabe6202.

(25) Piontek, A.; Bisz, E.; Szostak, M. Iron-Catalyzed Cross-Couplings in the Synthesis of Pharmaceuticals: In Pursuit of Sustainability. *Angew. Chem., Int. Ed.* **2018**, *57*, 11116−11128.

(26) Hubrich, J.; Himmler, T.; Rodefeld, L.; Ackermann, L. Ruthenium(II)-Catalyzed C−H Arylation of Azoarenes by Carboxylate Assistance. *ACS Catal.* **2015**, *5*, 4089−4093.

(27) Mining.com. https://www.mining.com/markets/ (accessed Feb 1, 2022).
(28) Egorova, K. S.; Ananikov, V. P. Which Metals are Green for Catalysis? Comparison of the Toxicities of Ni, Cu, Fe, Pd, Pt, Rh, and Au Salts. *Angew. Chem., Int. Ed.* **2016**, *55*, 12150−12162.
(29) Egorova, K. S.; Ananikov, V. P. Toxicity of Metal Compounds: Knowledge and Myths. *Organometallics* **2017**, *36*, 4071−4090.
(30) Li, S.-S.; Qin, L.; Dong, L. Rhodium-Catalyzed C−C Coupling Reactions via Double C−H Activation. *Org. Biomol. Chem.* **2016**, *14*, 4554−4570.
(31) Ackermann, L.; Vicente, R. Ruthenium-Catalyzed Direct Arylations Through C−H Bond Cleavages. In *C−H Activation*; Springer: Berlin, Heidelberg, 2010; Vol. *292*, pp 211−229.
(32) Gandeepan, P.; Müller, T.; Zell, D.; Cera, G.; Warratz, S.; Ackermann, L. 3d Transition Metals for C−H Activation. *Chem. Rev.* **2019**, *119*, 2192−2452.
(33) Bolm, C.; Legros, J.; Le Paih, J.; Zani, L. Iron-Catalyzed Reactions in Organic Synthesis. *Chem. Rev.* **2004**, *104*, 6217−6254.
(34) Correa, A.; García Mancheño, O.; Bolm, C. Iron-Catalysed Carbon−Heteroatom and Heteroatom−Heteroatom Bond Forming Processes. *Chem. Soc. Rev.* **2008**, *37*, 1108−1117.
(35) Bedford, R. B. How Low Does Iron Go? Chasing the Active Species in Fe-Catalyzed Cross-Coupling Reactions. *Acc. Chem. Res.* **2015**, *48*, 1485−1493.
(36) Bedford, R. B.; Brenner, P. B. The Development of Iron Catalysts for Cross-Coupling Reactions. In *Topics in Organometallic Chemistry*; Springer International Publishing, 2015; Vol. *50*, pp 19−46.
(37) Bauer, I.; Knölker, H.-J. Iron Catalysis in Organic Synthesis. *Chem. Rev.* **2015**, *115*, 3170−3387.
(38) Fürstner, A. Iron Catalysis in Organic Synthesis: A Critical Assessment of What It Takes To Make This Base Metal a Multitasking Champion. *ACS Cent. Sci.* **2016**, *2*, 778−789.
(39) Bisz, E.; Szostak, M. Iron-Catalyzed C−O Bond Activation: Opportunity for Sustainable Catalysis. *ChemSusChem* **2017**, *10*, 3964−3981.
(40) Shang, R.; Ilies, L.; Nakamura, E. Iron-Catalyzed C−H Bond Activation. *Chem. Rev.* **2017**, *117*, 9086−9139.
(41) Nakamura, E.; Yoshikai, N. Low-Valent Iron-Catalyzed C−C Bond Formation−Addition, Substitution, and C−H Bond Activation. *J. Org. Chem.* **2010**, *75*, 6061−6067.
(42) Halka, M.; Nordstrom, B. *Transition Metals*; Facts On File Inc.: New York, 2011; p 68.
(43) Ysart, G.; Miller, P.; Crews, H.; Robb, P.; Baxter, M.; L'Argy, C. D.; Lofthouse, S.; Sargent, C.; Harrison, N. Dietary Exposure Estimates of 30 Elements from the UK Total Diet Study. *Food Addit. Contam.* **1999**, *16*, 391−403.
(44) Cera, G.; Ackermann, L. Iron-Catalyzed C−H Functionalization Processes. *Top. Curr. Chem.* **2016**, *374*, No. 57.
(45) Doba, T.; Matsubara, T.; Ilies, L.; Shang, R.; Nakamura, E. Homocoupling-Free Iron-Catalysed Twofold C−H Activation/Cross-Couplings of Aromatics via Transient Connection of Reactants. *Nat. Catal.* **2019**, *2*, 400−406.
(46) Dombray, T.; Werncke, C. G.; Jiang, S.; Grellier, M.; Vendier, L.; Bontemps, S.; Sortais, J.-B.; Sabo-Etienne, S.; Darcel, C. Iron-Catalyzed C−H Borylation of Arenes. *J. Am. Chem. Soc.* **2015**, *137*, 4062−4065.
(47) Loup, J.; Zell, D.; Oliveira, J. C. A.; Keil, H.; Stalke, D.; Ackermann, L. Asymmetric Iron-Catalyzed C−H Alkylation Enabled by Remote Ligand meta-Substitution. *Angew. Chem., Int. Ed.* **2017**, *56*, 14197−14201.
(48) Mo, J.; Müller, T.; Oliveira, J. C. A.; Ackermann, L. 1,4-Iron Migration for Expedient Allene Annulations through Iron-Catalyzed C−H/N−H/C−O/C−H Functionalizations. *Angew. Chem., Int. Ed.* **2018**, *57*, 7719−7723.
(49) Mo, J.; Müller, T.; Oliveira, J. C. A.; Demeshko, S.; Meyer, F.; Ackermann, L. Iron-Catalyzed C−H Activation with Propargyl Acetates: Mechanistic Insights into Iron(II) by Experiment, Kinetics, Mössbauer Spectroscopy, and Computation. *Angew. Chem., Int. Ed.* **2019**, *58*, 12874−12878.
(50) Shaik, S. Iron opens up to high activity. *Nat. Chem.* **2010**, *2*, 347−349.
(51) Zhu, C.; Stangier, M.; Oliveira, J. C. A.; Massignan, L.; Ackermann, L. Iron-Electrocatalyzed C−H Arylations: Mechanistic Insights into Oxidation-Induced Reductive Elimination for Ferraelectrocatalysis. *Chem. - Eur. J.* **2019**, *25*, 16382−16389.
(52) Doba, T.; Ilies, L.; Sato, W.; Shang, R.; Nakamura, E. Iron-Catalysed Regioselective Thienyl C−H/C−H Coupling. *Nat. Catal.* **2021**, *4*, 631−638.
(53) Shang, R.; Ilies, L.; Nakamura, E. Iron-Catalyzed Directed C(sp2)−H and C(sp3)−H Functionalization with Trimethylaluminum. *J. Am. Chem. Soc.* **2015**, *137*, 7660−7663.
(54) Shang, R.; Ilies, L.; Nakamura, E. Iron-Catalyzed Ortho C−H Methylation of Aromatics Bearing a Simple Carbonyl Group with Methylaluminum and Tridentate Phosphine Ligand. *J. Am. Chem. Soc.* **2016**, *138*, 10132−10135.
(55) Jia, T.; Zhao, C.; He, R.; Chen, H.; Wang, C. Iron-Carbonyl-Catalyzed Redox-Neutral [4+2] Annulation of N−H Imines and Internal Alkynes by C−H Bond Activation. *Angew. Chem., Int. Ed.* **2016**, *55*, 5268−5271.
(56) Kimura, N.; Kochi, T.; Kakiuchi, F. Iron-Catalyzed Regioselective Anti-Markovnikov Addition of C−H Bonds in Aromatic Ketones to Alkenes. *J. Am. Chem. Soc.* **2017**, *139*, 14849−14852.
(57) Kimura, N.; Kochi, T.; Kakiuchi, F. Iron-Catalyzed Ortho-Selective C−H Alkylation of Aromatic Ketones with N-Alkenylindoles and Partial Indolylation via 1,4-Iron Migration. *Asian J. Org. Chem.* **2019**, *8*, 1115−1117.
(58) Messinis, A. M.; Finger, L. H.; Hu, L.; Ackermann, L. Allenes for Versatile Iron-Catalyzed C−H Activation by Weak O-Coordination: Mechanistic Insights by Kinetics, Intermediate Isolation, and Computation. *J. Am. Chem. Soc.* **2020**, *142*, 13102−13111.
(59) Kimura, N.; Katta, S.; Kitazawa, Y.; Kochi, T.; Kakiuchi, F. Iron-Catalyzed Ortho C−H Homoallylation of Aromatic Ketones with Methylenecyclopropanes. *J. Am. Chem. Soc.* **2021**, *143*, 4543−4549.
(60) Boddie, T. E.; Carpenter, S. H.; Baker, T. M.; DeMuth, J. C.; Cera, G.; Brennessel, W. W.; Ackermann, L.; Neidig, M. L. Identification and Reactivity of Cyclometalated Iron(II) Intermediates in Triazole-Directed Iron-Catalyzed C−H Activation. *J. Am. Chem. Soc.* **2019**, *141*, 12338−12345.
(61) DeMuth, J. C.; Song, Z.; Carpenter, S. H.; Boddie, T. E.; Radović, A.; Baker, T. M.; Gutierrez, O.; Neidig, M. L. Experimental and Computational Studies of the Mechanism of Iron-Catalysed C−H Activation/Functionalisation with Allyl Electrophiles. *Chem. Sci.* **2021**, *12*, 9398−9407.
(62) Bhatia, S.; Demuth, J. C.; Neidig, M. L. Intermediates and Mechanism in Iron-Catalyzed C−H Methylation with Trimethylaluminum. *Chem. Commun.* **2021**, *57*, 12784−12787.
(63) Ni, C.; Ellis, B. D.; Stich, T. A.; Fettinger, J. C.; Long, G. J.; Britt, R. D.; Power, P. P. Reduction of Terphenyl iron(II) or Cobalt(II) Halides in the Presence of Trimethylphosphine: an Unusual Triple Dehydrogenation of an Alkyl Group. *Dalton Trans.* **2009**, *310*, 5401−5405.
(64) Ray, K.; Bill, E.; Weyhermüller, T.; Wieghardt, K. Redox-Noninnocence of the S,S'-Coordinated Ligands in Bis(benzene-1,2-dithiolato)iron Complexes. *J. Am. Chem. Soc.* **2005**, *127*, 5641−5654.
(65) A tentative suggestion for the mechanism of formation of such complexes is presented in Section S5.1 of the Supporting Information.
(66) Beck, R.; Camadanli, S.; Flörke, U.; Klein, H.-F. Reaction cascade: Ortho-C−H Activation and C−C Coupling of Benzophenone Leading to Tetranuclear Organoiron and Mononuclear Organocobalt Complexes. *J. Organomet. Chem.* **2015**, *778*, 47−55.

https://doi.org/10.1021/acscatal.2c00772
ACS Catal. 2022, 12, 4947−4960

(67) Martínez-Carrión, A.; Howlett, M. G.; Alamillo-Ferrer, C.; Clayton, A. D.; Bourne, R. A.; Codina, A.; Vidal-Ferran, A.; Adams, R. W.; Burés, J. Kinetic Treatments for Catalyst Activation and Deactivation Processes based on Variable Time Normalization Analysis. *Angew. Chem., Int. Ed.* **2019**, *58*, 10189−10193.
(68) Temkin, O. N. Mechanisms of Formation of Catalytically Active Metal Complexes. In *Homogeneous Catalysis with Metal Complexes*; John Wiley & Sons: West Sussex, 2012; Vol. *32*, pp 453−544.
(69) Collman, J. P. Patterns of Organometallic Reactions Related to Homogeneous Catalysis. *Acc. Chem. Res.* **1968**, *1*, 136−143.
(70) Zhao, Q.; Meng, G.; Nolan, S. P.; Szostak, M. N-Heterocyclic Carbene Complexes in C−H Activation Reactions. *Chem. Rev.* **2020**, *120*, 1981−2048.
(71) Beck, R.; Sun, H.; Li, X.; Camadanli, S.; Klein, H. F. Cyclometalation of Thiobenzophenones with Mononuclear Methyl-iron and cobalt Complexes. *Eur. J. Inorg. Chem.* **2008**, *2008*, 3253−3257.
(72) Camadanli, S.; Beck, R.; Flörke, U.; Klein, H.-F. C−H Activation of Imines by Trimethylphosphine-Supported Iron Complexes and Their Reactivities. *Organometallics* **2009**, *28*, 2300−2310.
(73) Rathke, J. W.; Muetterties, E. L. Phosphine chemistry of iron(0) and (II). *J. Am. Chem. Soc.* **1975**, *97*, 3272−3273.
(74) Morris, R. H. Estimating the Acidity of Transition Metal Hydride and Dihydrogen Complexes by Adding Ligand Acidity Constants. *J. Am. Chem. Soc.* **2014**, *136*, 1948−1959.
(75) Karsch, H. H. Funktionelle Trimethylphosphinderivate, III. Ambivalentes Verhalten von Tetrakis(trimethylphosphin)eisen: Reaktion mit CO_2. *Chem. Ber.* **1977**, *110*, 2213−2221.
(76) Blom, B. *Reactivity of Ylenes at Late Transition Metal Centres*; Cuvillier Verlag: Göttingen, 2011; p 211.
(77) Jones, W. D. Isotope Effects in C−H Bond Activation Reactions by Transition Metals. *Acc. Chem. Res.* **2003**, *36*, 140−146.
(78) Chakraborty, S.; Guan, H. First-row Transition Metal Catalyzed Reduction of Carbonyl Functionalities: a Mechanistic Perspective. *Dalton Trans.* **2010**, *39*, 7427−7436.
(79) Bhattacharya, P.; Krause, J. A.; Guan, H. Iron Hydride Complexes Bearing Phosphinite-Based Pincer Ligands: Synthesis, Reactivity, and Catalytic Application in Hydrosilylation Reactions. *Organometallics* **2011**, *30*, 4720−4729.
(80) Yang, X. Unexpected Direct Reduction Mechanism for Hydrogenation of Ketones Catalyzed by Iron PNP Pincer Complexes. *Inorg. Chem.* **2011**, *50*, 12836−12843.
(81) Butschke, B.; Feller, M.; Diskin-Posner, Y.; Milstein, D. Ketone Hydrogenation Catalyzed by a new Iron(II)−PNN Complex. *Catal. Sci. Technol.* **2016**, *6*, 4428−4437.
(82) Bleith, T.; Gade, L. H. Mechanism of the Iron(II)-Catalyzed Hydrosilylation of Ketones: Activation of Iron Carboxylate Precatalysts and Reaction Pathways of the Active Catalyst. *J. Am. Chem. Soc.* **2016**, *138*, 4972−4983.
(83) Caldeweyher, E.; Bannwarth, C.; Grimme, S. Extension of the D3 Dispersion Coefficient Model. *J. Chem. Phys.* **2017**, *147*, No. 034112.
(84) Frisch, M. J.; Trucks, G. W.; Schlegel, H. B.; Scuseria, G. E.; Robb, M. A.; Cheeseman, J. R.; Scalmani, G.; Barone, V.; Petersson, G. A.; Nakatsuji, H.; Li, X.; Caricato, M.; Marenich, A. V.; Bloino, J.; Janesko, B. G.; Gomperts, R.; Mennucci, B.; Hratchian, H. P.; Ortiz, J. V.; Izmaylov, A. F.; Sonnenberg, J. L.; Williams; Ding, F.; Lipparini, F.; Egidi, F.; Goings, J.; Peng, B.; Petrone, A.; Henderson, T.; Ranasinghe, D.; Zakrzewski, V. G.; Gao, J.; Rega, N.; Zheng, G.; Liang, W.; Hada, M.; Ehara, M.; Toyota, K.; Fukuda, R.; Hasegawa, J.; Ishida, M.; Nakajima, T.; Honda, Y.; Kitao, O.; Nakai, H.; Vreven, T.; Throssell, K.; Montgomery, J. A., Jr.; Peralta, J. E.; Ogliaro, F.; Bearpark, M. J.; Heyd, J. J.; Brothers, E. N.; Kudin, K. N.; Staroverov, V. N.; Keith, T. A.; Kobayashi, R.; Normand, J.; Raghavachari, K.; Rendell, A. P.; Burant, J. C.; Iyengar, S. S.; Tomasi, J.; Cossi, M.; Millam, J. M.; Klene, M.; Adamo, C.; Cammi, R.; Ochterski, J. W.; Martin, R. L.; Morokuma, K.; Farkas, O.; Foresman, J. B.; Fox, D. J. *Gaussian 16*, revision A.03, Gaussian Inc.: Wallingford, CT, 2016.
(85) Grimme, S.; Antony, J.; Ehrlich, S.; Krieg, H.; Consistent, A. and Accurate ab Initio Parametrization of Density Functional Dispersion Correction (DFT-D) for the 94 Elements H-Pu. *J. Chem. Phys.* **2010**, *132*, No. 154104.
(86) Grimme, S.; Ehrlich, S.; Goerigk, L. Effect of the Damping Function in Dispersion Corrected Density Functional Theory. *J. Comput. Chem.* **2011**, *32*, 1456−1465.
(87) Marenich, A. V.; Cramer, C. J.; Truhlar, D. G. Universal Solvation Model Based on Solute Electron Density and on a Continuum Model of the Solvent Defined by the Bulk Dielectric Constant and Atomic Surface Tensions. *J. Phys. Chem. A* **2009**, *113*, 6378−6396.
(88) Tao, J.; Perdew, J. P.; Staroverov, V. N.; Scuseria, G. E. Climbing the Density Functional Ladder: Nonempirical Meta−Generalized Gradient Approximation Designed for Molecules and Solids. *Phys. Rev. Lett.* **2003**, *91*, No. 146401.
(89) Weigend, F. Accurate Coulomb-Fitting Basis Sets for H to Rn. *Phys. Chem. Chem. Phys.* **2006**, *8*, 1057−1065.
(90) Weigend, F.; Ahlrichs, R. Balanced Basis Sets of Split Valence, Triple Zeta Valence and Quadruple Zeta Valence Quality for H to Rn: Design and Assessment of Accuracy. *Phys. Chem. Chem. Phys.* **2005**, *7*, 3297−3305.
(91) Caldeweyher, E.; Ehlert, S.; Hansen, A.; Neugebauer, H.; Spicher, S.; Bannwarth, C.; Grimme, S. A Generally Applicable Atomic-Charge Dependent London Dispersion Correction. *J. Chem. Phys.* **2019**, *150*, No. 154122.

https://doi.org/10.1021/acscatal.2c00772
ACS Catal. 2022, 12, 4947−4960